JACS
JOURNAL OF THE AMERICAN CHEMICAL SOCIETY
Article
pubs.acs.org/JACS

# Circular Dichroism, Magnetic Circular Dichroism, and Variable Temperature Variable Field Magnetic Circular Dichroism Studies of Biferrous and Mixed-Valent *myo*-Inositol Oxygenase: Insights into Substrate Activation of $O_2$ Reactivity

Rae Ana Snyder,[†] Caleb B. Bell, III,[†] Yinghui Diao,[‡] Carsten Krebs,*[,‡,⊥] J. Martin Bollinger, Jr.,*[,‡,⊥] and Edward I. Solomon*[,†,§]

[†]Department of Chemistry, Stanford University, Stanford, California 94305, United States
[‡]Department of Biochemistry and Molecular Biology and [⊥]Department of Chemistry, The Pennsylvania State University, University Park, Pennsylvania 16802, United States
[§]Stanford Synchrotron Radiation Laboratory, SLAC, Stanford University, Menlo Park, California 94025, United States

Supporting Information

**ABSTRACT:** *myo*-Inositol oxygenase (MIOX) catalyzes the 4e$^-$ oxidation of *myo*-inositol (MI) to D-glucuronate using a substrate activated Fe(II)Fe(III) site. The biferrous and Fe(II)Fe(III) forms of MIOX were studied with circular dichroism (CD), magnetic circular dichroism (MCD), and variable temperature variable field (VTVH) MCD spectroscopies. The MCD spectrum of biferrous MIOX shows two ligand field (LF) transitions near 10000 cm$^{-1}$, split by ∼2000 cm$^{-1}$, characteristic of six coordinate (6C) Fe(II) sites, indicating that the modest reactivity of the biferrous form toward $O_2$ can be attributed to the saturated coordination of both irons. Upon oxidation to the Fe(II)Fe(III) state, MIOX shows two LF transitions in the ∼10000 cm$^{-1}$ region, again implying a coordinatively saturated Fe(II) site. Upon MI binding, these split in energy to 5200 and 11200 cm$^{-1}$, showing that MI binding causes the Fe(II) to become coordinatively unsaturated. VTVH MCD magnetization curves of unbound and MI-bound Fe(II)Fe(III) forms show that upon substrate binding, the isotherms become more nested, requiring that the exchange coupling and ferrous zero-field splitting (ZFS) both decrease in magnitude. These results imply that MI binds to the ferric site, weakening the Fe(III)−$\mu$-OH bond and strengthening the Fe(II)−$\mu$-OH bond. This perturbation results in the release of a coordinated water from the Fe(II) that enables its $O_2$ activation.

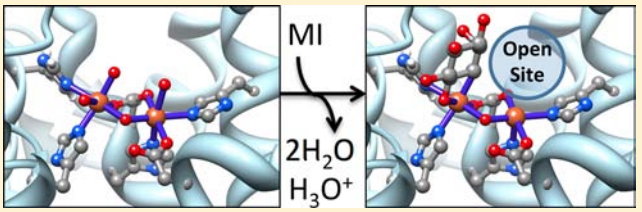


## INTRODUCTION

Ferritin-like, binuclear non-heme-iron enzymes (diiron enzymes that have a common four-helical bundle motif) are involved in a wide range of biochemical processes, many of which either have implications for human health or perform industrially important chemical transformations.[1−4] The diiron core of ribonucleotide reductase (RR) catalyzes the formation of a tyrosine radical that is required in the *de novo* synthesis of deoxyribonucleotides.[4,5] $\Delta^9$-Desaturase ($\Delta^9$D) catalyzes the insertion of a carbon−carbon double bond in stearoyl-acyl carrier protein (stearoyl-ACP), essential in the biosynthesis of oleic acid, the most abundant fatty acid in human adipose tissue.[6−8] The diiron site of methane monooxygenase (MMO) catalyzes the oxidation of methane, a green house gas,[9] to methanol, a usable fuel.[10−13] While *myo*-inositol oxygenase (MIOX), a eukaryotic/human enzyme that is essential to human health, also harbors a binuclear non-heme-iron cofactor,[14] it is structurally and mechanistically distinct from the ferritin-like diiron oxygenases and oxidases, such as RR, $\Delta^9$D, and MMO.[15−18]

MIOX catalyzes the 4e$^-$ oxidation of *myo*-inositol (MI) to D-glucuronate (DG).[17,19] This catalytic reaction forms a central part of the metabolic pathway of MI (Figure 1).[20−26] With roles in osmoregulation, membrane structure, signal transduction, and transcriptional regulation of hundreds of genes, the reactant (MI) has been implicated in affecting mood, reproduction, osteogenesis, the central nervous system, and insulin sensitivity.[19,23−25,27−36] It is a suggested treatment for various psychiatric and metabolic conditions, polycystic ovary syndrome and in the inhibition of certain types of cancer.[35,36] Its concentration is associated with glial proliferation, and it is thought to be a glial marker.[37,38] The product (DG) is of interest in biotechnology, specifically its incorporation into the backbones of polysaccharides (Figure 1).[39] In addition to the important medical implications of the substrate (MI) and the biotech applications of the product (DG), diabetic complications have been attributed to an increase in MIOX expression and activity, making the enzyme a potential drug target.[31]

Most binuclear non-heme-iron enzymes, including RR, $\Delta^9$D, and MMO, have diiron sites that are housed in four-$\alpha$-helical

Received: July 9, 2013
Published: September 25, 2013

   dx.doi.org/10.1021/ja406635k | J. Am. Chem. Soc. 2013, 135, 15851−15863

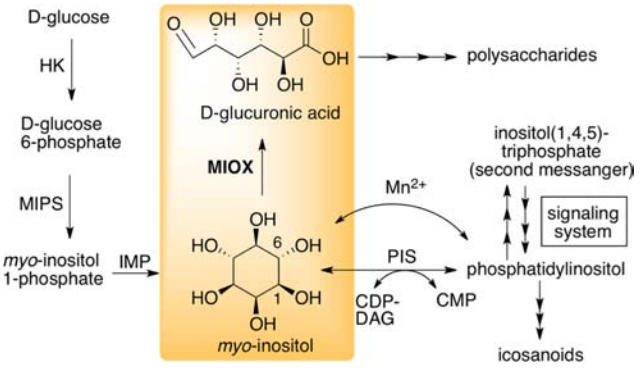


**Figure 1.** Metabolic pathway of *myo*-inositol.[20−26] The oxygenation of *myo*-inositol to D-glucuronate, catalyzed by MIOX, is highlighted. Abbreviations: HK, hexokinase; MIPS, *myo*-inositol-1-phosphate synthase; IMP, inositol monophosphate phosphatase; PIS, phosphatidylinositol synthase; CDP-DAG, cytidine diphosphate diacylglycerol; CMP, cytidine monophosphate.

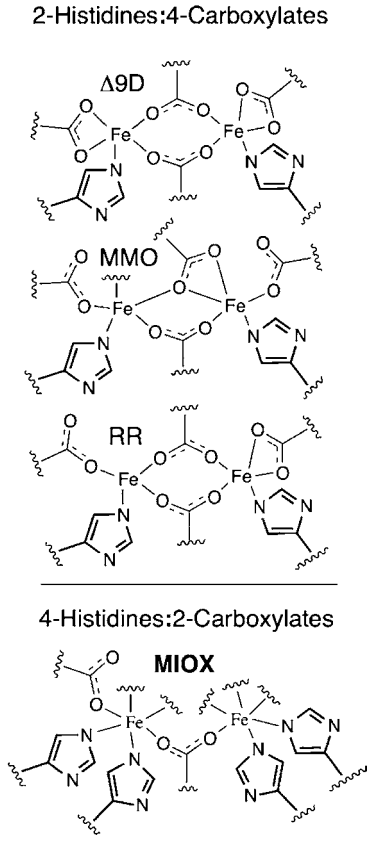


**Figure 2.** Protein derived ligand sets of ferritin-like binuclear non-heme-iron enzymes[1,2,5,7,8,11,12,40] (top) and MIOX[16−18] (bottom).

bundle motifs and coordinated by two histidines and four carboxylates from protein derived ligand sets (Figure 2, top).[1,2,5,7,8,11,12,40] They are active in the Fe(II)Fe(II) state (Figure 3, top).[1,41−48] They activate $O_2$ by a $2e^-$ reduction, forming bridged peroxy-Fe(III)Fe(III) intermediates and catalyze two-electron oxidations. MIOX, however, deviates from these commonly shared characteristics among diiron enzymes. The diiron cofactor is housed in an HD-domain (named after a conserved histidine and aspartate residue doublet), where five helices contribute a four-histidine/two-carboxylate ligand set (Figure 2, bottom).[16−18] It is, to date, the only member of the HD-domain protein structural superfamily known to possess a diiron cluster and oxygenase activity (although a recent report suggests that there may be more examples).[49] Although MIOX can exist in three oxidation states (Fe(II)Fe(II), Fe(II)Fe(III), and Fe(III)Fe(III)), the Fe(II)Fe(III) form is catalytically active (Figure 3, bottom), and substrate must first bind to the active site before $O_2$ activation occurs.[27,28] Putatively, the substrate coordinates to the Fe(III) site of the cofactor via its C1 and C6 alkoxides (Figure 1). While the outer-sphere $1e^-$ reduction of $O_2$ is thermodynamically difficult ($E$ = −160 mV),[50] MIOX undergoes an oxidative addition of $O_2$ to the Fe(II) to form a superoxo-Fe(III) species (Figure 3, bottom), intermediate G.[17,27] Intermediate G initiates MI oxidation by cleavage of the C1−H bond.[27] Steps in the catalysis of MIOX following hydrogen abstraction from C1 are less well characterized but are thought to involve one of the following: homolysis of the O−O bond followed by substrate/hydroxyl radical recombination, transfer of the hydroperoxyl moiety to the substrate radical, or generation of a ketone intermediate, which is attacked by the (hydro)peroxo moiety.[17,51] Understanding the reactivity of this unusual enzyme at the molecular level offers fundamental insight into how a binuclear non-heme-iron center may be tuned to use a $1e^-$ rather than $2e^-$ reduction strategy for $O_2$ activation and has the potential to aid in the development of new diabetic therapies and glucuronic acid based polysaccharides for biotech applications.

These studies elucidate several fundamental features of the MIOX reaction. These features include the unusual lack of catalytic activity of the Fe(II)Fe(II) state, as well as the modest $O_2$ reactivity of this form ($k \approx 2 \times 10^3\ M^{-1}\ s^{-1}$; 100-fold less than that of the Fe(II)Fe(III)·MI form),[27,52] and the necessity for substrate addition to the mixed-valent Fe(II)Fe(III) species for $O_2$ activation. Circular dichroism (CD), magnetic circular dichroism (MCD), and variable temperature variable field (VTVH) MCD studies of MIOX in its Fe(II)Fe(II), Fe(II)Fe(III), and Fe(II)Fe(III)·MI states are presented and provide structural and mechanistic insight into these requirements for $O_2$ activation.

Near IR CD/MCD is especially useful for studying the high-spin $d^6$ Fe(II) center in biferrous, Fe(II)Fe(III), and Fe(II)Fe(III)·MI forms of MIOX. Non-heme ferrous sites are generally inaccessible through EPR and absorption spectroscopies, making them difficult to study.[1] Near IR CD/MCD spectroscopies, however, allow for the observation of ferrous ligand field (LF) transitions, which are weak in absorption but relatively intense in CD and MCD.[1,53] The energies of these correlate to different coordination geometries. A six-coordinate (6C) Fe(II) site will exhibit two LF transitions near 10000 $cm^{-1}$, split by ∼2000 $cm^{-1}$. These transitions undergo a larger splitting in a 5C square pyramidal geometry, giving rise to one band at >10000 $cm^{-1}$ and the other at ∼5000 $cm^{-1}$. For a 5C trigonal bipyramidal site, these bands shift to <10000 $cm^{-1}$ and <5000 $cm^{-1}$. For a 4C tetrahedral site, two transitions are present in the 5000−7000 $cm^{-1}$ region.

Transitions involving the Fe(III) in the Fe(II)Fe(III) forms of MIOX may also be accessible with near IR CD/MCD spectroscopies. Weak spin-forbidden Fe(III) $^6A_1 \rightarrow {}^4T_1$ and $^6A_1 \rightarrow {}^4T_2$ LF transitions may be observed due to exchange coupling between the irons and mixing with intense charge-transfer transitions.[54−62] These transitions decrease in energy with increasing ligand-field strength, with LF transitions of 4C Fe(III) sites at highest energy and those of 6C sites at lowest energy. In addition, the mixed-valent forms of MIOX could also


dx.doi.org/10.1021/ja406635k | J. Am. Chem. Soc. 2013, 135, 15851−15863

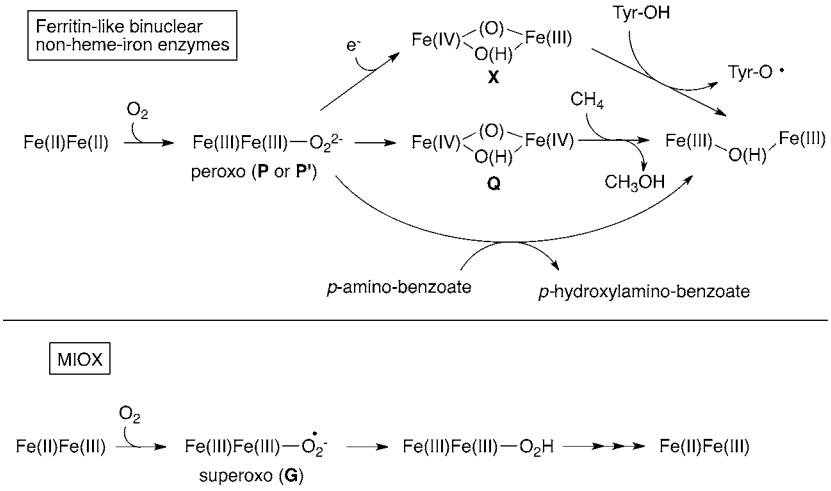


**Figure 3.** Comparison of the mechanistic strategies of most binuclear non-heme-iron enzymes[1,41−48] (top) and MIOX[16−18,27,28] (bottom).

have an intervalence charge-transfer (IT, Fe(II) → Fe(III)) transition, which would contribute to the near IR region of the spectrum but is expected to have little MCD intensity (because these are strongly polarized along the Fe−Fe bond and MCD C-term intensity requires two perpendicular transition moments).[54,62−64]

VTVH MCD methodology is also a valuable probe of the ground states of the coupled binuclear Fe sites in both the Fe(II)Fe(II) and Fe(II)Fe(III) forms of MIOX. It allows for analysis of the spin system and determination of important spin-Hamiltonian parameters, specifically the exchange coupling ($J$) between the Fe ions, which reflects the nature of the bridging ligands, and the zero-field splittings (ZFSs) of each of the Fe ions, which provide information complementary to that obtained from CD/MCD spectra about the nature of the ligand field at each Fe site.[1,54,62]

As presented below, the combined CD, MCD, and VTVH MCD approach provides insights into the geometric and electronic structures and, thus, the reactivities of the Fe(II)Fe(II) and Fe(II)Fe(III) sites and the role of MI binding in activating the enzyme for $O_2$ addition to the cofactor. They generate a model where high histidine ligation results in a coordinatively saturated Fe(II)Fe(II) site. Oxidation to the Fe(II)Fe(III) state allows for MIOX to bind MI, which modifies a bridge and results in an open coordination position at the Fe(II) for the activation of $O_2$ by $1e^-$. This mechanism is in sharp contrast to that of the ferritin-like diiron oxygenases and oxidases, which react from the biferrous state with open coordination positions on both irons allowing $2e^-$ reductive activation of $O_2$ to form a peroxo-bridge.

## EXPERIMENTAL SECTION

**Materials.** $FeSO_4·6H_2O$ was obtained from J.T. Baker. Bis-tris buffer, MI, acetic acid, and sucrose were obtained from Sigma-Aldrich. Deuterium oxide ($D_2O$; 99.9% $^2H$) and perdeuterated glycerol ($d_8$-glycerol; 98% $^2H$) were obtained from Cambridge Isotope Laboratories (Andover, MA). Both MI and sucrose were dissolved in $D_2O$ and lyophilized before use. $N_2$(g) (ultrahigh purity) for the glovebox and Ar(g) (99.9%) for Schlenk line manipulations were obtained from Praxair. $N_2$(l) and He(l) were also obtained from Praxair. Deoxygenated deuterated buffer (50 mM bis-tris·acetate in $D_2O$ with 10 wt %/wt $d_8$-glycerol and pD 6.0) was prepared by multiple freeze−pump−thaw cycles on a Schlenk line with Ar(g). Deoxygenated protein was prepared (on ice) by multiple (6+) gentle vacuum/purge cycles followed by purging the sample's headspace with Ar(g) for 3+ hours.

**Preparation of Apo-MIOX.** Apo *Mus musculus* kidney MIOX was expressed, purified, and quantified according to published procedures.[14] Apo-MIOX was exchanged into deuterated buffer (50 mM bis-tris·acetate in $D_2O$ with 10 wt %/wt $d_8$-glycerol, pD 6.0) by 8+ cycles of 4× dilution with $D_2O$ buffer and concentration back to 2−3 mM. The concentration was determined by the absorption band at 280 nm ($\varepsilon$ = 60800 $M^{-1}$ $cm^{-1}$).[14] Protein was kept at 5−10 °C during buffer exchange. The voltage associated with the absorption of the CD spectrum of the apoprotein was checked at 1500 nm (~6700 $cm^{-1}$) to monitor the buffer exchange.

**Preparation of Biferrous MIOX (MIOX(II,II)).** Deoxygenated apo-MIOX in deuterated buffer was brought into the glovebox and kept at 7 °C on a cold plate while 1.70 equiv of deoxygenated ferrous ammonium sulfate (in deuterated buffer) was added. Fe(II) loading was confirmed by near IR CD.

**Preparation of Biferric MIOX (MIOX(III,III)).** MIOX(II,II) (~1−2 mM) was treated with excess $O_2$ by diluting the sample with an $O_2$ containing buffer (~4 °C, ~300−400 $\mu$M of $O_2$)[65] to 30 $\mu$M and leaving it in an aerobic atmosphere (~4 °C) for 8 h. MIOX(III,III) samples were then concentrated to 2−3 mM. Complete oxidation to MIOX(III/III) by this protocol was verified by Mössbauer spectroscopy after MI addition (see Figure S13 (middle) in the Supporting Information).

**Preparation of Mixed-Valent Fe(II)Fe(III) MIOX (MIOX(II,III)).** Equimolar amounts of deoxygenated MIOX(II,II) and MIOX(III,III) were mixed in an anaerobic environment (glovebox) and incubated for 1 h at 7 °C. Mössbauer spectra taken on samples prepared according to this protocol and then treated with saturating MI showed 60−70% conversion to the mixed-valent species with equal quantities (15−20%) of biferrous and biferric components (see Figure S13 (bottom) in the Supporting Information).

**Preparation of MI Complexes of MIOX.** MIOX·MI samples (1−3 mM) were prepared by adding (anaerobically for MIOX(II,III)·MI and MIOX(II,II)·MI and aerobically for MIOX(III,III)·MI) a small volume (10−20 $\mu$L) of a concentrated MI solution to the MIOX samples for final MI concentrations of 50−100 mM.

**Instrumentation.** Near IR (600−1900 nm region) CD and MCD spectroscopies were performed on a JASCO J730D spectropolarimeter with an $N_2$(l) cooled InSb detector. The MCD and VTVH MCD data for the 800−500 nm region were collected on a JASCO J810 spectropolarimeter equipped with a photomultiplier tube that has an S1 photocathode. For CD spectroscopy, a circulator connected to the CD cell holder was used to cool the anaerobic quartz CD cell. For MCD spectroscopy, a He(l) cooled Oxford Instrument SM4000 7T-superconducting magnet was used for field and temperature variation. An Agilent 8453 UV−visible spectrophotometer was used to determine protein concentrations.

**CD and MCD Spectroscopy.** All CD experiments were performed in an anaerobic quartz cell at 4 °C. CD titrations were performed by adding 120 $\mu$L of deoxygenated apo-MIOX to the anaerobic quartz cell


dx.doi.org/10.1021/ja406635k | J. Am. Chem. Soc. 2013, 135, 15851−15863

in a glovebox. For each addition of ferrous ammonium sulfate (at 0, 0.25, 0.5, 0.75, 1, 1.25, 1.5, 1.75, 2, 2.5, and 3 equiv of Fe(II)), a CD spectrum was taken after a 15−20 min incubation. MCD samples were prepared by adding sucrose to saturation and separating out any solid sucrose through centrifugation in a glovebox. A CD spectrum was taken after sucrose addition to confirm that it did not perturb the diiron site (see Figures S3 and S5 in Supporting Information). Sucrose-saturated samples were then added to MCD cells in the glovebox and immediately transferred to $N_2$(l). MCD spectra were taken at ±7, ±5, ±3, ±1, and 0 T at 2 K and ±7 and 0 T for temperatures of 5, 10, and 20 K. The MCD baseline was corrected by averaging positive and negative fields (e.g., ((+7 T) − (−7 T))/2). CD and MCD spectra were analyzed by a nonlinear least-squares fitting procedure to resolve them into the minimum number of Gaussian bands required to fit both data sets while allowing for limited sharpening and shifting of peaks in the MCD (taken at low temperature). For both the CD and MCD spectra reported, multiple scans (5−20) were averaged.

**VTVH MCD Spectroscopy.** VTVH MCD data were taken at 10600 and 8500 $cm^{-1}$ for MIOX(II,II) and MIOX(II,II)·MI and at 17600 $cm^{-1}$ for MIOX(II,III) and MIOX(II,III)·MI. Data were taken at fields of 0, ±0.35, ±0.7, ±1.4, ±2.1, ±2.8, ±3.5, ±4.2, ±4.7, ±5.6, ±6.3, and ±7.0 T and for temperatures of 2, 3, 5, 7.5, 10, 15, 20, and 25 K. MCD intensity was averaged over 100−200 scans for each field at each temperature. The reported data points are baseline-subtracted averages of the measurements for positive and negative field taken at the same temperature (their error bars represent the propagation of errors from the standard deviations). The reduced chi-squared value was used to judge the goodness of fit for the VTVH MCD data. The VTVH MCD data were fit with doublet and spin projection models as described in the Results and Analysis section.[53,66]

## RESULTS AND ANALYSIS

**MIOX(II,II).** The binding of Fe(II) to apo-MIOX in the absence of $O_2$ was investigated with near-IR (NIR) CD spectroscopy at 4 °C. Two positive bands at ∼10000 $cm^{-1}$ grew in together with added Fe (Figure S1a, Supporting Information). These features saturated at ∼2 equiv of Fe(II) (Figure S1b, Supporting Information). Least squares fitting of the titration curve at 10100 $cm^{-1}$ (Figure S1a, insert) to eq S1, Supporting Information, gave an Fe(II) dissociation constant ($K_D$) of 0.2 mM, similar in magnitude to that of $\Delta^9$D (0.8 mM).[7] The CD spectrum of biferrous MIOX (MIOX(II,II)) showed no perturbation upon the addition of *myo*-inositol (MI) in substantial excess (25:1), with the relative intensities and peak positions of the bands unchanged (Figure 4a). The two bands in the CD spectrum of MIOX(II,II) were Gaussian resolved into bands with energies of 8500 and 10300 $cm^{-1}$ and were unaltered upon the addition of the glassing agent, sucrose (Figure S3, Supporting Information).

Similarly, the NIR MCD spectrum of MIOX(II,II) taken at low temperature (2 K) and high field (7 T) was Gaussian resolved into two bands at 8600 and 10400 $cm^{-1}$ (Figure 4b). These bands correlate well with those in the CD, with slight differences in energy and diminished line widths due to the lower temperature for MCD (2 K vs 4 °C). As in CD, the addition of MI did not perturb these spectral features (Figure 4b). The NIR CD and MCD spectral features are attributed to d → d transitions for a biferrous site. The CD and MCD spectra of MIOX(II,II) lack any features <8000 $cm^{-1}$, and thus, the biferrous site does not contain a 4C or 5C square pyramidal Fe(II) center.[1,53] The presence of a band at 10400 $cm^{-1}$ indicates that at least one of the Fe(II) ions is 6C. The VTVH MCD results below distinguish between the 6C and 5C trigonal bipyramidal geometries possible for the second Fe(II).

VTVH MCD data were taken on biferrous MIOX at 8500 and 10500 $cm^{-1}$ (Figure 4b, arrows) and show that the signals

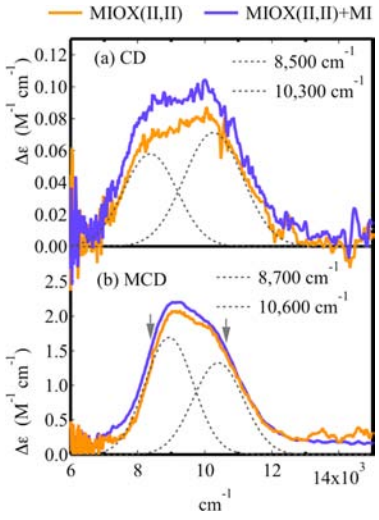


**Figure 4.** The CD and MCD spectra of MIOX(II,II). Spectra include without (orange) and with (purple) the addition of MI (25-fold excess) for the (a) CD and (b) MCD of biferrous MIOX. The gray arrows in panel b indicate where the VTVH MCD was taken. Protein concentrations were 1−2 mM.

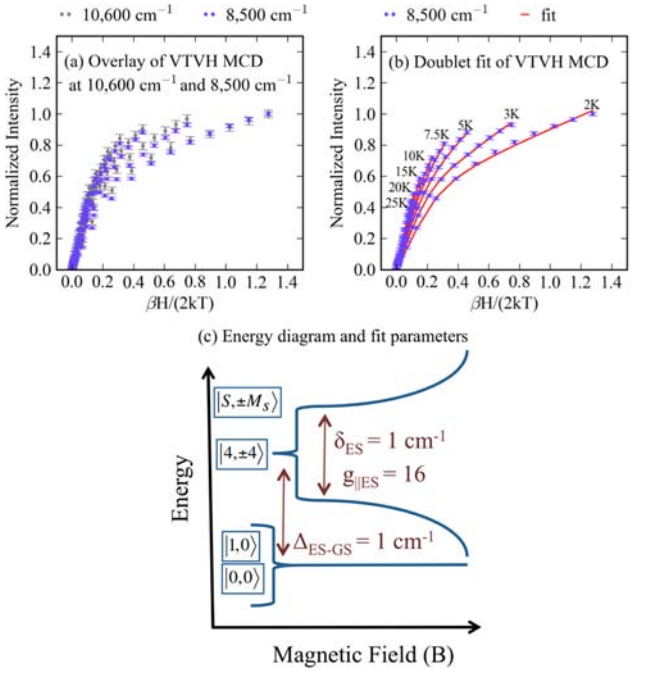


**Figure 5.** The VTVH MCD of MIOX(II,II). For biferrous MIOX (2 mM), panel a shows overlay of the VTVH MCD at 8500 $cm^{-1}$ (blue) and 10600 $cm^{-1}$ (gray), panel b shows the fit of the VTVH MCD (data in blue, fit in red), and panel c shows the energy diagram of the doublet fit, including fit parameters.

decrease with increasing temperature (Figure 5a), confirming that the bands are associated with MCD C-terms.[67] No perturbation of the VTVH MCD saturation magnetization curves is observed upon addition of MI (Figure S2a,b, Supporting Information). The VTVH MCD data taken at both 8500 and 10500 $cm^{-1}$ overlay (Figure 5a), indicating that the intensities of the two bands have equal contributions from both Fe(II) sites. If a 5C trigonal bipyramidal Fe(II) site were present, it would contribute intensity to the <10000 $cm^{-1}$ band and would


dx.doi.org/10.1021/ja406635k | J. Am. Chem. Soc. 2013, 135, 15851−15863

result in different VTVH MCD behaviors at 8500 and 10500 $cm^{-1}$.[1,53] Thus, both Fe(II) ions are 6C.

The VTVH MCD data of an integer-spin system may be fit according to a non-Kramers doublet model in which the total MCD intensity is given by the sum of contributions from the different sublevels of the spin manifold of the biferrous site (eq 1).[1,53,68,69]

$$\Delta\varepsilon = \sum_i \left[ (A_{sat})_i \left( \int_0^{\pi/2} \frac{\cos^2\theta \sin\theta}{\Gamma_i} g_{\|_i} \beta \mathbf{H} \alpha_i \, d\theta - \sqrt{2} P \int_0^{\pi/2} \frac{\sin^3\theta}{\Gamma_i} g_{\perp_i} \beta \mathbf{H} \alpha_i \, d\theta \right) + B_i \mathbf{H} \gamma_i \right] \quad (1)$$

where

$$\Gamma_i = \sqrt{{\delta_i}^2 + (g_{\|_i}\beta\mathbf{H}\cos\theta)^2 + (g_{\perp_i}\beta\mathbf{H}\sin\theta)^2},$$

$$\alpha_i = \frac{\exp\left[-\frac{E_i - \frac{\Gamma_i}{2}}{kT}\right] - \exp\left[-\frac{E_i + \frac{\Gamma_i}{2}}{kT}\right]}{\sum_j \left( \exp\left[-\frac{E_j - \frac{\Gamma_j}{2}}{kT}\right] + \exp\left[-\frac{E_j + \frac{\Gamma_j}{2}}{kT}\right] \right)},$$

$$\gamma_i = \frac{\exp\left[-\frac{E_i - \frac{\delta_i}{2}}{kT}\right] + \exp\left[-\frac{E_i + \frac{\delta_i}{2}}{kT}\right]}{\sum_j \left( \exp\left[-\frac{E_j - \frac{\delta_j}{2}}{kT}\right] + \exp\left[-\frac{E_j + \frac{\delta_j}{2}}{kT}\right] \right)}$$

The MCD contribution from the $i$th doublet is described in terms of C-term ($(A_{sat})_i$) and B-term ($B_i$) intensities, rhombic dimer zero-field splitting (ZFS) ($\delta_i$), dimer **g**-values ($g_{\perp_i}$ and $g_{\|_i}$), and energy $E_i$. The linear B-term allows for the mixing between different doublets induced by the applied magnetic field **H**. The factors $\alpha_i$ and $\gamma_i$ allow for the Boltzmann population over the spin manifold at a given temperature $T$ where $k$ is the Boltzmann constant; $P = M_z/M_{x,y}$, where $M_z$ and $M_{x,y}$ are the transition dipole moments for the indicated direction. This model assumes that only one chromophore contributes to the MCD intensity at a given energy. Equation 1 can be modified to account for $m$ chromophores contributing to the VTVH MCD intensity at a given energy (where each chromophore has a different $(A_{sat})_i$, $B_i$, and $P$) by substituting these with

$$(A_{tot})_i = \sum_m (A_{sat})_m, \quad (P_{tot})_i = \frac{1}{(A_{tot})_i} \sum_m (A_{sat})_m (P)_m, \quad (B_{tot})_i = \sum_m B_m$$

This modified equation was employed to fit the VTVH MCD data in Figure 5a. Initial fits fixed the polarization ratios and $g_\perp$ to zero. Treating the polarization ratios and $g_\perp$ as adjustable parameters and allowing them to deviate from zero did not improve the fit. The best fit (Figure 5b, red line) requires two singlet sublevels lowest in energy and a doublet excited state ($\Delta_{ES\text{-}GS}$) at 1 $cm^{-1}$ with $g_{\|_{ES}} = 16$ and $\delta_{ES} = 1$ $cm^{-1}$. Inclusion of a second excited state did not significantly improve the fit. These results (Figure 5c) indicate that two $M_s = 0$ levels are at the lowest energy and a sublevel with $M_s = \pm 4$ is the lowest lying excited state.

High spin Fe(II) has $S = 2$ and $M_s = \pm 2, \pm 1, 0$, which will split due to axial ($D$) and rhombic ($E$) ZFS. Additionally, the two irons interact through superexchange pathways provided by bridging ligands, which results in $S_{tot} = |S_1 + S_2| \ldots |S_1 - S_2| = 4, 3, 2, 1, 0$ levels split by $8J$, $6J$, $4J$, and $2J$ ($H_{ex} = -2J\hat{S}_1\cdot\hat{S}_2$, where $J$ quantifies the exchange coupling). The combined effects of exchange coupling and axial and rhombic ZSF for each Fe(II) ion and the Zeeman effect can be described by the spin-Hamiltonian in eq 2, which acts on the $|S_1, S_2, M_{s_1}, M_{s_2}\rangle$ uncoupled basis sets of Fe1 and Fe2.[1]

$$\begin{aligned} H = &-2J\hat{S}_1\cdot\hat{S}_2 + D_1\left(\hat{S}_{z_1}{}^2 - \frac{1}{3}S_1(S_1+1)\right) \\ &+ E_1(\hat{S}_{x_1}{}^2 - \hat{S}_{y_1}{}^2) + D_2\left(\hat{S}_{z_2}{}^2 - \frac{1}{3}S_2(S_2+1)\right) \\ &+ E_2(\hat{S}_{x_2}{}^2 - \hat{S}_{y_2}{}^2) + g_{x_1}\beta H_x\hat{S}_{x_1} + g_{y_1}\beta H_y\hat{S}_{y_1} \\ &+ g_{z_1}\beta H_z\hat{S}_{z_1} + g_{x_2}\beta H_x\hat{S}_{x_2} + g_{y_2}\beta H_y\hat{S}_{y_2} + g_{z_2}\beta H_z\hat{S}_{z_2} \end{aligned} \quad (2)$$

The relationship from LF theory between the **g**-values of the Zeeman terms ($g_{x_1}\beta H_x\hat{S}_{x_1}$, $g_{y_1}\beta H_y\hat{S}_{y_1}$, ...) and $D$ and $E$ for an Fe(II) ion is given by eqs 3a and 3b, where $\lambda$ is the ground state spin–orbit coupling constant (−100 $cm^{-1}$ for Fe(II)), and $k^2$ is the Steven's orbital reduction factor (<1 due to covalency).

$$D_{Fe(II)} = \frac{-k^2\lambda}{4}(g_{xFe(II)} + g_{yFe(II)} - 2g_{zFe(II)}) \quad (3a)$$

$$E_{Fe(II)} = \frac{-k^2\lambda}{4}(g_{yFe(II)} - g_{xFe(II)}) \quad (3b)$$

Applying eq 2 to the uncoupled ferrous basis set results in a 25 × 25 matrix, with eigenvectors and eigenvalues giving the spin-state wave functions and their energies for the coupled biferrous site. The ferrous $|D|$ values were constrained to be ≤15 $cm^{-1}$, the maximum observed in model systems and ligand field calculations, and $|E/D|$ values were constrained to be ≤1/3. This spin Hamiltonian analysis shows that two $M_s = 0$ ground sublevels and a low-lying $M_s = \pm 4$ ($g' = 16$) sublevel (as in Figure 5c) occur when $D_1$, $D_2$, and $J$ are all negative and $J$ is small. The $J/D$ correlation diagram for this case is given in Figure 6. In this diagram ($D_1 = D_2 = -10$ $cm^{-1}$ and $E_1 = E_2 = 0$), two $M_s = 0$ sublevels are lowest in energy and an $M_s = \pm 4$ sublevel excited state is next in energy when $-3 < J < 0$ $cm^{-1}$. Allowing $E/D$ ratios to be 1/3 mixes the spin wave functions, splits the doublets, and alters the energies. The final fit shows that both Fe(II) sites have similar values of $D$ (−8 to −12 $cm^{-1}$) and $E/D$ (0.18 and 0.2) and are weakly antiferromagnetically coupled ($J = -0.1$ $cm^{-1}$).

Table 1 summarizes the parameters from this doublet fit, the results of the spin-Hamiltonian analysis of MIOX(II,II) and their comparison to equivalent data on reduced $\Delta^9$D, another binuclear ferrous enzyme with a similar spin manifold in the ground state. In the case of reduced $\Delta^9$D, the $g = 16$ doublet excited state is significantly higher in energy (10.6 $cm^{-1}$ compared with 1 $cm^{-1}$) correlating to a larger $-J$, resulting in a field-induced crossover of the ground state to be observable as an inflection point in the lowest temperature isotherm of the VTVH MCD data.[7] While no inflection point is present in the VTVH MCD data of MIOX(II,II) in Figure 5b, a $g = 16$ EPR signal was observed in previous studies.[14] Because the VTVH MCD data cannot be fit with a $g = 16$ ground state, the EPR data support the presence of a $g_{\|} = 16$ low lying excited state. The final result with two negative ZFS of similar values ($D$'s = −8 to −12 $cm^{-1}$) is


dx.doi.org/10.1021/ja406635k | J. Am. Chem. Soc. 2013, 135, 15851−15863

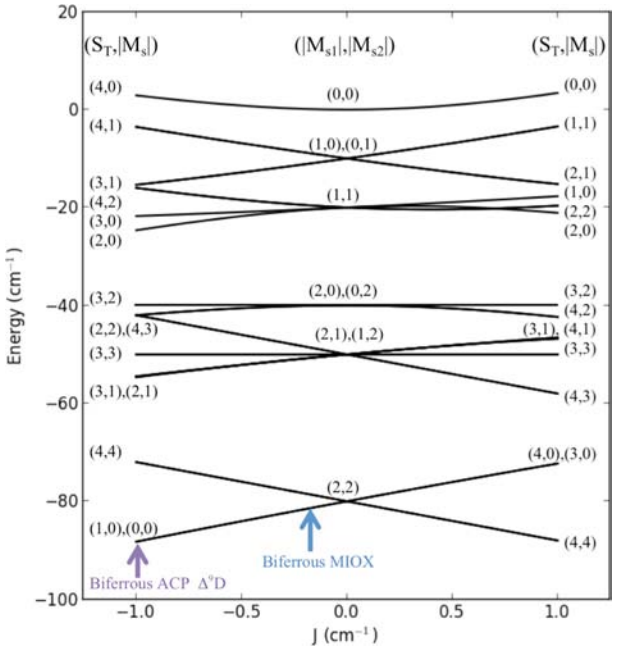


**Figure 6.** The correlation diagram for a coupled Fe(II) system with both ions having negative ZFS. Correlation diagram includes only the zero-field energy levels for a coupled $S_1 = S_2 = 2$ system (eq 3 where $H_{x,y,z} = 0$) with $D_1 = D_2 = -10$ cm$^{-1}$ and $(E/D)_1 = (E/D)_2 = 0$. The exchange coupling ($J$) is varied from +1 to −1 cm$^{-1}$. The middle represents the energy splitting for only ZFS contributions (thus, an uncoupled system). The left and right sides represent antiferromagnetic ($J < 0$) and ferromagnetic ($J > 0$) interactions. The relative positions of biferrous MIOX and ACP $\Delta^9$D are indicated by the blue and purple arrows.

consistent with the assignment of two similar 6C Fe(II) sites.[1] The small antiferromagnetic coupling constant eliminates the possibility of a hydroxo bridge but is consistent with the presence of one or more $\mu$-1,3-carboxylate bridge(s).[1]

The CD, MCD, and VTVH MCD data of MIOX(II,II) and their analysis reveal a biferrous site with both Fe(II) ions coordinated by six ligands and bridged by one or more carboxylates. No change was observed upon the addition of excess MI, suggesting that MI does not bind to MIOX(II,II).

**MIOX(II,III) CD and MCD.** The mixed-valent form of MIOX was investigated by near IR CD and MCD spectroscopy. MIOX(II,III) samples were formed via the comproportionation of equal quantities of biferric and biferrous MIOX upon mixing them in the absence of $O_2$ to give equal concentrations. The final product was a mixture of mixed-valent (60−70%) and equal quantities (15−20%) of the biferric and biferrous forms (quantification based on Mössbauer data taken after MI addition, see Figure S13 in Supporting Information). Figure 7a shows the CD spectrum of this mixture (in black) overlaid with the spectra of the pure biferrous (in red) and biferric (in green) forms, all collected at 5 °C. Intense negative ∼8000 and positive ∼11000 cm$^{-1}$ features are present in the spectrum of the sample containing the mixed-valent form. These features do not appear in the spectrum of either the biferrous or biferric form, and are, therefore, associated with the MIOX(II,III) species present in the mixture. Quantitative subtraction of the biferric and biferrous components from the spectrum and renormalization (Figure 7c) leads to little difference. Sucrose does not perturb the CD spectrum (Figure S5, Supporting Information), which could be Gaussian resolved into two bands at 8200 and 11200 cm$^{-1}$ (Figure 7c).

The NIR MCD spectrum of the mixed-valent mixture was taken at 7 T and 2 K (Figure 7b, black). The mixed-valent mixture exhibits two negative features near ∼8000 and ∼11000 cm$^{-1}$ that do not appear in the spectrum of either the biferrous (Figure 7b, red) or biferric (Figure 7b, green) form. These features, therefore, belong to MIOX(II,III). Quantitative subtraction of the biferrous and biferric MCD components and renormalization shows that the two negative bands are the only features present in the MCD spectrum of MIOX(II,III) (Figure 7d). These features resolve into Gaussian peaks at 8400 and 11000 cm$^{-1}$, which correlate with those in the CD spectrum. The decrease in the width and small shift in energy are associated with the lower temperature of the MCD experiment. Previous EPR studies on mouse MIOX indicate the presence of only one mixed-valent species, and thus, both bands are associated with the same species.[14] Possible near IR transitions for binuclear

**Table 1. Summary of the Doublet Fit and Spin Hamiltonian Parameters for Biferrous MIOX and ACP $\Delta^9$D**

| | | | MIOX[a] | ACP $\Delta^9$D[b] |
|---|---|---|---|---|
| doublet fit parameters | $M_s = \pm 4$ | $g_{\parallel_{ES}}$ | 16.0 | 16.0 |
| | | $\delta_{ES}$ (cm$^{-1}$) | 1.0 | 2.07 |
| | | $A_{tot}$ | 1.0 | 1.6 |
| | | B-term (%$A_{tot}$) | −2.3 | −3 |
| | | energy (cm$^{-1}$) | 1.1 | 10.6 |
| | $M_s = 0$ | B-term (arb) | 1.31 | 0.08 |
| | | energy (cm$^{-1}$) | 0 | 1.97 |
| | $M_s = 0$ | B-term (arb) | 1.06 | 0.02 |
| | | energy (cm$^{-1}$) | 0 | 0 |
| Spin Hamiltonian Parameters | | $J$ (cm$^{-1}$) | −0.1 | −1.0 |
| | | $D_1$ (cm$^{-1}$) | −8 to −12 | −5 to −15 |
| | | $(E/D)_1$ | 0.18 | |
| | | $D_2$ (cm$^{-1}$) | −8 to −12 | −5 to −15 |
| | | $(E/D)_2$ | 0.2 | |

[a]This work. [b]Reference 7.


dx.doi.org/10.1021/ja406635k | J. Am. Chem. Soc. 2013, 135, 15851−15863

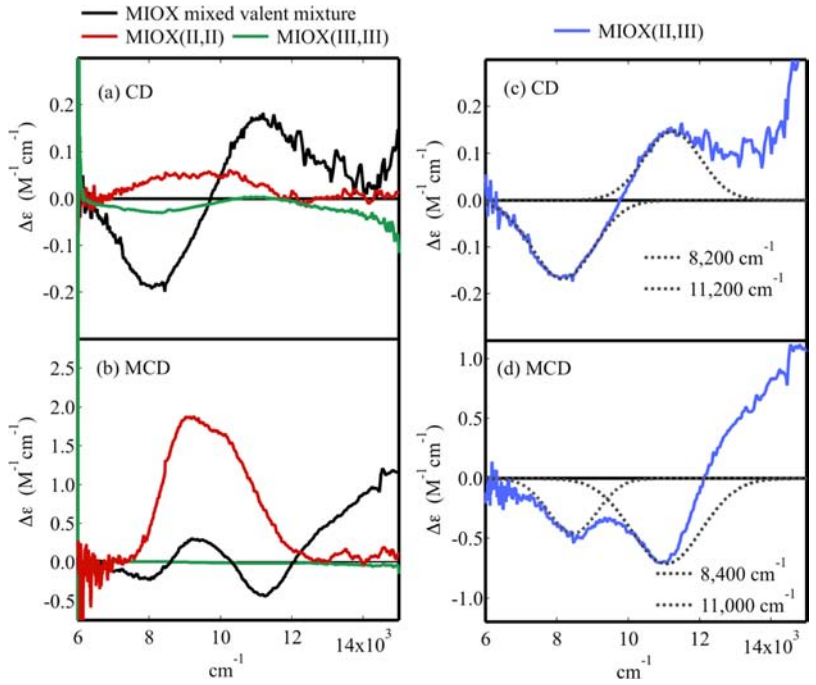


**Figure 7.** The CD and MCD of MIOX(II,III). The spectra of the mixed-valent MIOX mixture (black), MIOX(II,II) (red), and MIOX(III,III) (green) are overlaid for (a) CD and (b) MCD. Subtraction of biferric and biferrous contaminants gives the (c) CD and (d) MCD of MIOX(II,III), which are Guassian resolved (gray). Protein concentrations were 1−3 mM.

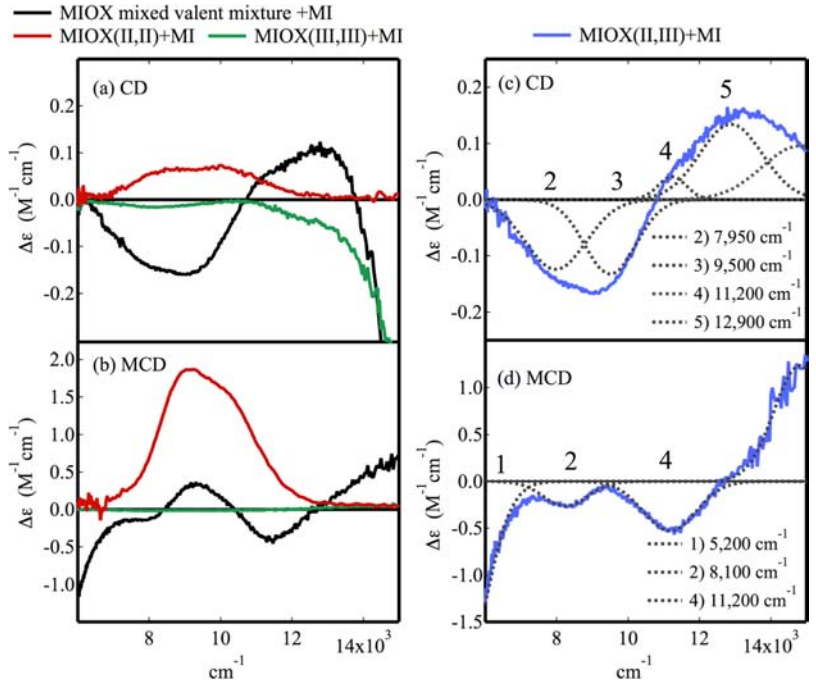


**Figure 8.** The CD and MCD of MIOX(II,III)·MI. The spectra of the mixed-valent MIOX mixture (black) and biferrous (red) and biferric (green) MIOX taken after addition of MI are overlaid for (a) CD and (b) MCD. Subtraction of the biferric and biferrous contaminants gives the (c) CD and (d) MCD of MIOX(II,III)·MI, which are Guassian resolved (gray). Protein concentrations were 1−3 mM with 25-fold excess MI.

mixed-valent iron include ferrous and ferric d → d and intervalence charge transfer (IT) transitions. However, ferrous d → d transitions are expected to dominate the MCD spectrum because ferric d → d transitions are spin-forbidden and IT transitions have low MCD intensity. Both the ∼8000 and ∼11000 $cm^{-1}$ bands are observed in the CD and MCD spectra with significant intensity and are thus assigned as Fe(II) d → d transitions. Any IT or Fe(III) d → d transition present in this region would be obscured by these intense Fe(II) d → d bands. The band of lowest energy is observed at ∼8000 $cm^{-1}$, eliminating the possibility of 4C or 5C geometries.[1,53] The transitions are centered ∼10000 $cm^{-1}$, which is consistent with a 6C site. Their larger than expected splitting of ∼2600−3000 $cm^{-1}$ indicates the presence of a weakly bound (likely $H_2O$) ligand.


dx.doi.org/10.1021/ja406635k | J. Am. Chem. Soc. 2013, 135, 15851−15863

Figure 8a shows the effects of MI addition on the NIR CD spectrum (at 4 °C) of the mixed-valent mixture (black). At least four bands are observed, one negative feature with a shoulder and one positive feature also with a shoulder. Given the intensities of these features, none appear to be present in the overlaid spectrum of either MIOX(II,II)·MI (Figure 8a, red) or MIOX(III,III)·MI (Figure 8a, green), indicating that they may arise from only the mixed-valent form. Subtraction of the biferrous and biferric components and renormalization gives the spectrum of MIOX(II,III)·MI in Figure 8c, which resolves into four Gaussian bands labeled 2−5 (band 1 is observed at lower energy in the MCD spectrum, *vide infra*). The $K_D$ value of MI (0.7 ± 0.3 mM)[17] would suggest full conversion to the bound form under the experimental conditions (51 mM MI concentration), and a higher MI concentration does not alter the CD spectrum (Figure S9, Supporting Information). Because the previous EPR study also does not indicate the presence of more than one mixed-valent species for MI-bound MIOX, bands 2−5 in the CD spectrum in Figure 8c are attributed to a single MI-bound MIOX(II,III) species.[14]

The MCD spectrum of the mixed-valent mixture with added MI taken at 7 T and 2 K is shown in Figure 8b (black). Three negative features at ∼5500, ∼8000, and ∼11000 $cm^{-1}$ in the mixed-valent mixture are not present in the MCD spectra of either MIOX(II,II)·MI or MIOX(III,III)·MI (red and green overlay). Thus, these features are attributed to the MIOX(II,III)·MI species. Subtraction of the biferrous and biferric components and renormalization give the MCD spectrum of MIOX(II,III)·MI (Figure 8d). Gaussian fits show that these bands (labeled 1, 2, and 4) are positioned at 5200, 8100, and 11200 $cm^{-1}$. Thus, MIOX(II,III)·MI has a total of five bands in the combined NIR CD and MCD spectra (Figure 8c,d, bands 1−5). Two LF bands are associated with Fe(II), and thus, the other three transitions must be either spin-forbidden d → d (which gain intensity via exchange coupling and mixing with nearby CT bands) or IT transitions. Band 1 is assigned to a Fe(II) d → d transition because it is intense in the MCD and at <7000 $cm^{-1}$ (inconsistent with Fe(III) LF transitions).[54,62−64] This assignment requires that Fe(II) is either 4C or 5C square pyramidal.[1,70] Band 2 at 7950 $cm^{-1}$ is assigned as a $^6A_1 \rightarrow {}^4T_1$ Fe(III) spin-forbidden d → d transition because it correlates to an ∼8000 $cm^{-1}$ band in the NIR CD of MIOX(III,III)·MI (Figure S10, Supporting Information), which has only spin-forbidden d → d transitions in this region. The low energy of this high-spin Fe(III) $^6A_1 \rightarrow {}^4T_1$ transition indicates a strong ligand field and thus a 6C Fe(III) site.[54,62−64] These assignments leave band 4, the only other NIR MCD feature, to be assigned as the other Fe(II) d → d transition. Thus, the Fe(II) site in MIOX(II,III)·MI has ligand field transitions at 5200 and 11200 $cm^{-1}$ and has a 5C square pyramidal geometry. Band 3 in the CD spectrum has no MCD intensity and no corresponding band in the biferric form. Thus, it likely arises from an IT transition.

Band 5 may arise from either an IT transition or another component of an Fe(III) spin-forbidden LF transition. In addition to the lower-energy bands, there is also a shoulder at ∼14500 $cm^{-1}$ in the extended MCD spectrum of MIOX(II,III)·MI (Figure S11, Supporting Information). It is unlikely to arise from an IT transition (because it appears in the MCD); its intensity is comparable to LF transitions, but its energy is too high for an Fe(II) LF transition. Its energy and intensity are consistent with a 6C Fe(III) $^6A_1 \rightarrow {}^4T_2$ transition (5C Fe(III) $^6A_1 \rightarrow {}^4T_2$ transitions are at >16100 $cm^{-1}$).[54,62−64] It is likely that IT and Fe(III) LF transitions are also present in the MIOX(II,III) spectra in Figure 7 but are obscured by the intense Fe(II) LF transitions of the 6C site. A summary of band assignments is given in Table 2. The CD and MCD spectra of MIOX(II,III) and MIOX(II,III)·MI show that the ferrous site converts from a 6C to a 5C square pyramidal geometry upon the addition of MI.

**Table 2. Summary of CD and MCD Gaussian bands for the CD and MCD of MIOX(II,III)·MI**

| bands | assignment | energy in CD ($cm^{-1}$) | energy in MCD ($cm^{-1}$) |
|---|---|---|---|
| 1 | Fe(II) d → d ($z^2$) | – | 5200 |
| 2 | Fe(III) d → d ($^6A_1 \rightarrow {}^4T_1$) | 8100 | 7950 |
| 3 | IT | 9500 | – |
| 4 | Fe(II) d → d ($x^2 - y^2$) | 11200 | 11200 |
| 5 | IT or Fe(III) d → d | 12900 | – |

**MIOX(II,III) VTVH MCD.** Obtaining VTVH MCD on the LF transitions of MIOX(II,III) forms is precluded by the presence of the overlaying bands from the biferrous contaminant. VTVH MCD data were therefore taken without and with MI bound on a band in the charge-transfer region (a ligand → Fe(III) CT) at 17600 $cm^{-1}$ (Figure S11, Supporting Information) where the biferrous and biferric species do not contribute (Figure 9). The

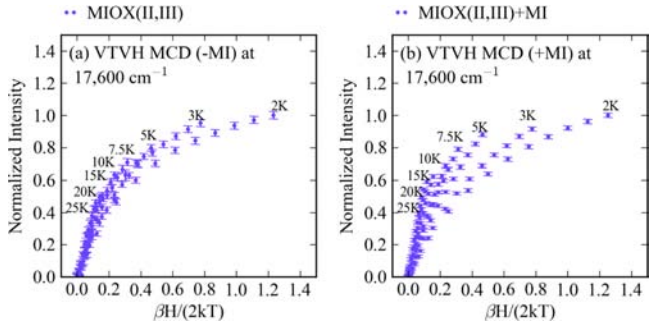


**Figure 9.** The VTVH MCD of MIOX(II,III) and MIOX(II,III)·MI. The VTVH MCD was taken at 17600 $cm^{-1}$ for MIOX(II,III) (1−2 mM) (a) without MI and (b) with MI (25-fold excess).

VTVH MCD data of the mixed-valent MIOX forms were fit using eq 1 applied to an Fe(II)Fe(III) site. The antiferromagnetic coupling of the Fe(III) ion with $S = 5/2$ and the Fe(II) ion with $S = 2$ results in an $S_{tot} = 1/2$ Kramer's doublet ground state (thus, $\delta_i = 0$ in eq 1). The lowest-temperature isotherm was fit with the ground state $g_{\|}$ (1.95 for MIOX(II,III) and MIOX(II,III)·MI) and $g_{\perp}$ (1.66 for MIOX(II,III); 1.81 for MIOX(II,III)·MI) taken from EPR data.[14] $M_z/M_{x,y}$, $(A_{sat})_0$, and $B_0$ were adjustable parameters. Fitting the isotherms also required the inclusion of the excited doublet state with $g_{\|} = 6.00$ and $g_{\perp} = 0.00$ (Figure 10a) for both MIOX(II,III) and MIOX(II,III)·MI forms. The best fits are shown in Figure 10b (for MIOX(II,III)) and Figure 10c (for MIOX(II,III)·MI) with fit parameters listed in Table 3. The optimized fits showed the presence of an excited state at ∼28 $cm^{-1}$ for MIOX(II,III) and at ∼17 $cm^{-1}$ for MIOX(II,III)·MI. Inclusion of a third excited doublet did not significantly improve either fit. These data indicate that the excited state for both MIOX(II,III) and MIOX(II,III)·MI is an $M_s = \pm 3/2$ doublet.

A high-spin ferric center has a $^6A_1$ ground state with $S = 5/2$. Coupling this center to a high-spin ferrous ($S = 2$) center results in $S_{tot} = 9/2$, $7/2$, $5/2$, $3/2$, and $1/2$ states. The exchange interaction splits these levels by $9J$, $7J$, $5J$, and $3J$. All but the $S_{tot} =$


dx.doi.org/10.1021/ja406635k | J. Am. Chem. Soc. 2013, 135, 15851−15863

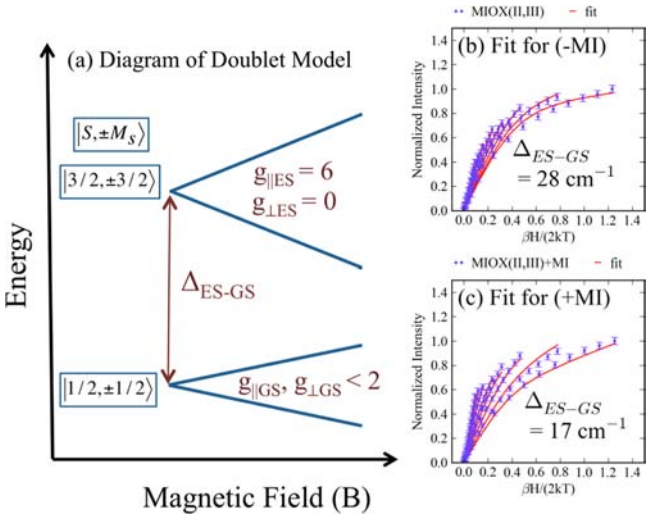


**Figure 10.** Doublet fits for the VTVH MCD of MIOX(II,III) and MIOX(II,III)·MI: (a) diagram of the doublet model used for fitting the VTVH MCD taken at 17600 $cm^{-1}$ for MIOX(II,III) (1−2 mM) and fits (b) without MI and (c) with MI (25-fold excess).

**Table 3. Summary of the Doublet Fit Parameters for MIOX(II,III) without and with MI**

| spin wave function | doublet parameters | −MI | +MI |
|---|---|---|---|
| $M_s = \pm 3/2$ | $g_{\parallel_{ES}}$ | 6.0 | 6.0 |
| | $g_{\perp_{ES}}$ | 0 | 0 |
| | $A_{sat}$ | 15.8 | 1.7 |
| | $M_z/M_{x,y}$ | 0.33 | 0.35 |
| | B-term (%$A_{sat}$) | −2.8 | 0.2 |
| | energy ($cm^{-1}$) | 28 | 17 |
| $M_s = \pm 1/2$ | $g_{\parallel_{GS}}$ | 1.95 | 1.95 |
| | $g_{\perp_{GS}}$ | 1.66 | 1.81 |
| | $A_{sat}$ | 13.8 | 24.0 |
| | $M_z/M_{x,y}$ | 0.33 | 0.35 |
| | B-term (%$A_{sat}$) | 0.2 | 0.3 |
| | energy ($cm^{-1}$) | 0 | 0 |

1/2 split due to ZFS with a magnitude and sign dictated by the ferrous site (the ferric contribution is small, that is, $|D_{Fe(II)}| \gg |D_{Fe(III)}|$).[1] Applying eq 2 to the uncoupled $|S_1,M_1,S_2,M_2\rangle$ Fe(II)Fe(III) system produces a 30 × 30 matrix, with eigenvectors and eigenvalues giving the sublevel wave functions and their energies. The energy level diagram for this system is given in Figure 11, where $W$ is the energy of the states and the ZFS of the ferric center is neglected ($D_{Fe(III)}$) = 0). The doublet fits for both MIOX(II,III) and MIOX(II,III)·MI indicate an $S_{tot}$ = 3/2 excited state with its $M_s = \pm 3/2$ component lowest in energy. This situation occurs only when $D_{Fe(II)}/J < 0$. Given that Fe(II) and Fe(III) are antiferromagnetically coupled ($S_{tot}$ = 1/2, thus $J <$ 0) in both MIOX(II,III) and MIOX(II,III)·MI, $D_{Fe(II)}$ is positive for both species. Values of $|D_{Fe(II)}/J|$ of ∼0.40 and ∼0.34 are estimated for MIOX(II,III) and MIOX(II,III)·MI, respectively, using Figure 11 and the excited state energies from the doublet fits. Estimates of the values of $D_{Fe(II)}$ can be obtained from eq 3a with the values of $g_{Fe(II)}$ calculated from the EPR-determined dimer **g**-values using vector coupling ($g_{dimer} = 7/3g_{Fe(III)} - 4/3g_{Fe(II)}$), where values of $g_{Fe(III)}$ are assumed to be 2.0023 with $k^2$ = 0.8 and $\lambda = -100$ $cm^{-1}$.[54,62,71] This analysis gives values of

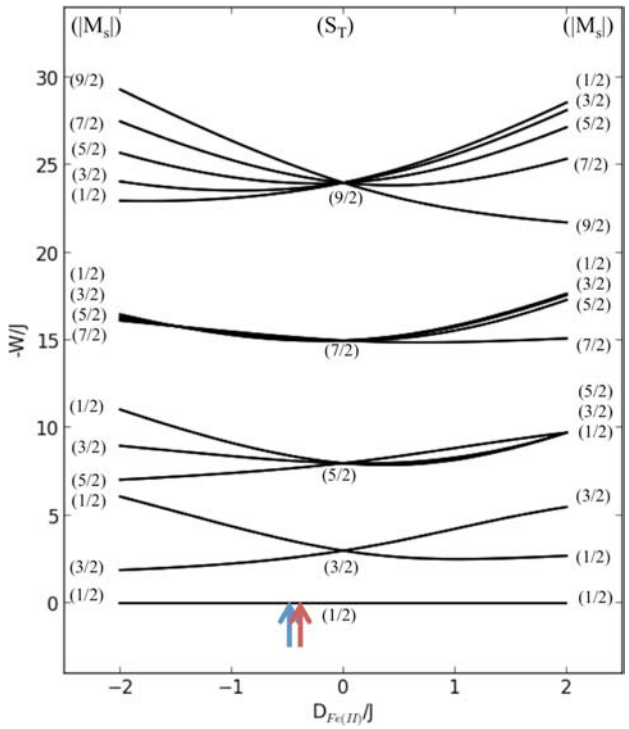


**Figure 11.** The correlation diagram for a Fe(II)Fe(III) system. The $D_{Fe(II)}/J$ energy correlation diagram is for a coupled $S_1$ = 2 and $S_2$ = 5/2 system at zero-field (eq 3). $D_{Fe(III)}$ and $E/D$ values were set to zero. The relative positions for MIOX without and with MI are indicated by the blue and red arrows, respectively.

$D_{Fe(II)}$ of 4.2 and 2.2 $cm^{-1}$ for MIOX(II,III) and MIOX(II,III)·MI, respectively. From these values, one can calculate values of $J$ of −10.5 and −6.5 $cm^{-1}$ for MIOX(II,III) and MIOX(II,III)·MI, respectively.

These spin-Hamiltonian parameters can be more accurately determined (without the assumption of eq 3, which considers only the contributions of $\Delta S$ = 0 excited states to the ZFS) by directly fitting eq 2 to the VTVH MCD data using a spin projection model (spin projection of the Fe(III) in the Fe(II)Fe(III) site).[66] Equation 4 uses the spin-expectation values of the different spin sublevels defined by eq 2 to compute MCD intensities ($\Delta\varepsilon$):

$$\frac{\Delta\varepsilon}{E} = \frac{\gamma}{4\pi S}\int_0^{\pi}\int_0^{2\pi}\sum_i N_i(l_x\langle S_x\rangle_i M_{yz}^{eff} + l_y\langle S_y\rangle_i M_{xz}^{eff} + l_z\langle S_z\rangle_i M_{xy}^{eff})\sin(\theta)\,d\theta\,d\phi r \quad (4)$$

where $S$ is the spin of the system, $E$ is the energy of the source, $\gamma$ is a collection of constants, $\langle S_x\rangle_i$, $\langle S_y\rangle_i$, and $\langle S_z\rangle_i$ are spin expectation values for the $i$th spin sublevel in the indicated direction with Boltzmann population, $N_i$, $l_x$, $l_y$, and $l_z$ are directional vectors associated with the propagation of light relative to the molecular axis, and $M_{yz}^{eff}$, $M_{xz}^{eff}$, and $M_{xy}^{eff}$ are the effective transition-moment products. Previous VTVH MCD fitting to eq 4 utilized a simplex routine to sample solution space. This routine is inefficient and may find a local, rather than global, minimum. To improve sampling of solution space and ensure a global search, a genetic algorithmic approach was developed (section 2 in Supporting Information). Optimized spin-Hamiltonian parameters for MIOX(II,III) and MIOX(II,III)·MI are provided in Table 4, and the best fits are shown in Figure 12a,b. It should be noted that all parameters were allowed to vary


dx.doi.org/10.1021/ja406635k | J. Am. Chem. Soc. 2013, 135, 15851−15863

**Table 4. Summary of the Spin Hamiltonian Parameters from the Spin Projection Fits of MIOX(II,III) without and with MI**

| | spin Hamiltonian parameters | −MI | +MI |
|---|---|---|---|
| | $J$ ($cm^{-1}$) | −12.3 | −8.6 |
| Fe(II) ZFS and Zeeman parameters | $D$ ($cm^{-1}$) | 5.9 | 3.9 |
| | $E/D$ | 0.11 | 0.02 |
| | $g_x$ | 2.27 | 2.10 |
| | $g_y$ | 2.15 | 2.10 |
| | $g_z$ | 2.07 | 2.05 |
| Fe(III) ZFS and Zeeman parameters | $D$ ($cm^{-1}$) | 0.01 | 0.21 |
| | $E/D$ | 0.01 | 0.04 |
| | $g_x$ | 2.00 | 2.00 |
| | $g_y$ | 2.00 | 2.00 |
| | $g_z$ | 2.00 | 2.00 |

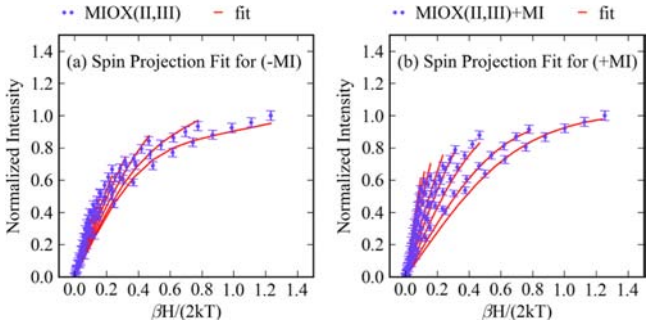


**Figure 12.** Spin projection fits for the VTVH MCD of MIOX(II,III) and MIOX(II,III)·MI. The fits are shown in red and are for the VTVH MCD taken at 17600 $cm^{-1}$ for MIOX(II,III) (1−2 mM) (a) without and (b) with MI (25-fold excess).

in the fitting routine, except for the principal **g**-values of the Fe(III) site, which were fixed at 2.0023. Initial fitting attempts assumed an axial Fe(II) center (i.e., $E/D = 0$ and $g_x = g_y$), as previously indicated by EPR studies. While the VTVH MCD data of MIOX(II,III)·MI were fit satisfactorily with an axial model, those for MIOX(II,III) required some rhombic character. For MIOX(II,III), the fit gives $J = -12.3$ $cm^{-1}$, $D_{Fe(III)} = 0.01$ $cm^{-1}$, $D_{Fe(II)} = 5.9$ $cm^{-1}$, and $(E/D)_{Fe(II)} = 0.11$ with $g_{xFe(II)} = 2.27$ $g_{yFe(II)} = 2.15$ and $g_{zFe(II)} = 2.07$. Values of **g** were calculated for the ground state doublet of the Fe(II)Fe(III) site with these spin-Hamiltonian parameters and found to be $g_z = 1.94$, $g_y = 1.71$, and $g_y = 1.55$. The EPR spectrum for mouse MIOX(II,III) shows a sharp $g_{\|} = 1.95$ signal and a broad $g_{\perp} = 1.66$ signal.[14] The breadth of the $g_{\perp}$ signal had previously been attributed to **g**-strain. The $g_x$ and $g_y$ values obtained from this spin projection fit are positioned well within the EPR spectral envelope (Figure S12, Supporting Information). For MIOX(II,III)·MI, $J = -8.6$ $cm^{-1}$, $D_{Fe(III)} = 0.21$ $cm^{-1}$, and $D_{Fe(II)} = 3.9$ $cm^{-1}$ with $g_{\perp Fe(II)} = 2.10$ and $g_{\|Fe(II)} = 2.05$. Doublet dimer **g**-values were calculated to be $g_{\|} = 1.96$ and $g_{\perp} = 1.80$, consistent with experiment ($g_{\|} = 1.95$ and $g_{\perp} = 1.81$).[14] Thus, upon MI binding, the magnitudes of both $J$ and $D_{Fe(II)}$ decrease.

Upon MI addition, the $D_{Fe(II)}$ of MIOX(II,III) decreases from 5.9 to 3.9 $cm^{-1}$ and $-J$ decreases from 12.3 to 8.6 $cm^{-1}$. The values of $J$ indicate that the Fe(II) and Fe(III) are bridged by a $\mu$-$OH^-$ in both forms.[1] The decrease in $-J$ suggests that the $OH^-$ bridge is weakened upon MI binding. The decrease in $D_{Fe(II)}$ is related to the geometry change of the Fe(II) center.[53] Axial distortions will split the $t_{2g}$ set of d-orbitals into the $d_{xz,yz}$ and the $d_{xy}$ levels. For the positive $D_{Fe(II)}$ found experimentally, the $d_{xy}$ orbital is lower in energy, and $D_{Fe(II)}$ is inversely proportional to the energy difference between the $d_{xy}$ and the $d_{xz,yz}$ levels. Removing a ligand from the 6C Fe(II) would increase this energy splitting and decrease $D_{Fe(II)}$. Thus, the decrease in $D_{Fe(II)}$ observed experimentally is consistent with the results from the MCD spectra that the Fe(II) site undergoes a change from 6C to 5C geometry upon binding of MI.

The CD- and MCD-derived excited-state splittings and the VTVH MCD derived ground-state splittings show that upon the addition of MI, the 6C Fe(II) in MIOX(II,III) loses a weak (water) ligand to become 5C. The exchange coupling, $J$, also decreases, indicating that the MI binding weakens the hydroxo bridge.

## DISCUSSION

The CD, MCD, and VTVH MCD data show that biferrous MIOX has two Fe(II) centers with ligand field transitions at ~10000 $cm^{-1}$ split by ~2000 $cm^{-1}$ and similar values of ZFS. Thus, both Fe(II) sites are 6C. The VTVH MCD analysis also shows weak antiferromagnetic coupling (−0.1 $cm^{-1}$), which

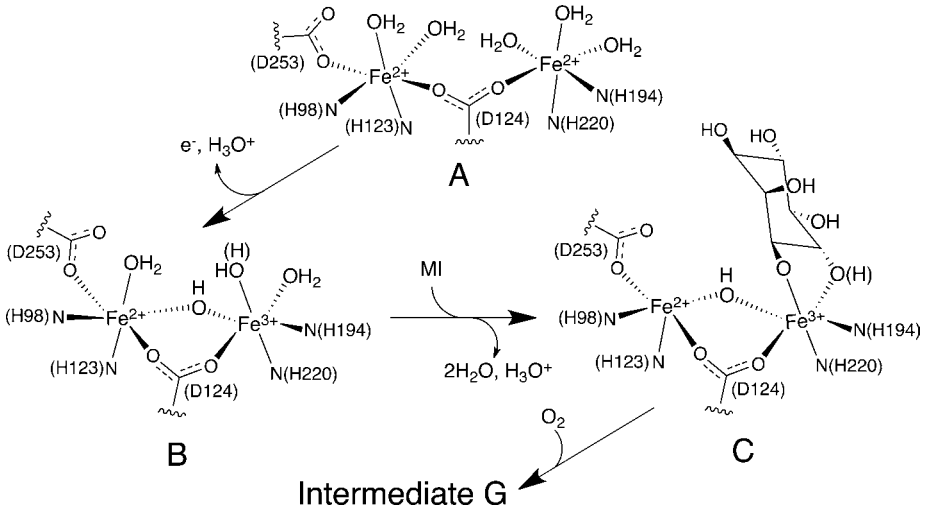


**Figure 13.** Proposed structural models for (A) MIOX(II,II), (B) MIOX(II,III), and (C) MIOX(II,III)·MI.


dx.doi.org/10.1021/ja406635k | J. Am. Chem. Soc. 2013, 135, 15851−15863

indicates the presence of only $\mu$-1,3-bridging carboxylates. MI addition does not perturb the spectra of MIOX(II,II), indicating that it does not bind. The crystallographic data for oxidized (biferric or mixed-valent) MIOX show that the protein contributes two histidine ligands to each Fe, a monodentate carboxylate ligand to one of the Fe ions, and a $\mu$-1,3-carboxylate bridge.[16,18] The spectroscopic and crystallographic data indicate that biferrous MIOX has the structure illustrated in Figure 13A with solvent completing the coordination spheres of both ferrous centers. Most biferrous proteins have weak $\mu$-1,3-carboxylate bridges that are inefficient superexchange pathways for electron transfer between the Fe(II) sites. $O_2$ thus must bridge the two irons in order to be activated by an inner-sphere $2e^-$ reduction. This mechanism requires open coordination sites on each Fe(II) center. While the biferrous species of MIOX has the weak $\mu$-1,3-carboxylate bridge, it is coordinatively saturated with no open positions for $O_2$ to bridge. These structural aspects account for its modest reactivity toward $O_2$. This reaction has an associated rate constant ($k \approx 2 \times 10^3$ $M^{-1}$ $s^{-1}$) 50-fold less than the rate constant for the productive combination of MIOX(II,III)·MI with $O_2$ ($k \approx 10^5$ $M^{-1}$ $s^{-1}$) and generates only the inactive biferric state, possibly by an outer-sphere process.

The CD and MCD spectra of mixed-valent MIOX show two features (at ~8000 and ~11000 $cm^{-1}$) with VTVH MCD analysis showing a $D_{Fe(II)} \approx 6$ $cm^{-1}$ with some rhombicity (E/D $\approx$ 0.11). These data are consistent with a 6C Fe(II) site with a weakly bound water ligand. The VTVH MCD analysis also gives a $-J$ of 12 $cm^{-1}$, which requires a hydroxo-bridge between the Fe(II) and Fe(III) centers. These spectroscopic data (and crystallographic data for protein ligation)[16,18] suggest that MIOX(II,III) has the structure in Figure 13B. MIOX(II,III) in the absence of substrate is also slow to react with dioxygen and is oxidized to the biferric state without $O_2$ activation. These spectroscopic results suggest that the unreactive nature of MIOX(II,III) can also be attributed to the saturated coordination (6C) of the Fe(II) center, preventing its inner-sphere activation of $O_2$.

Upon MI addition, the Fe(II) LF features are strongly perturbed. In MIOX(II,III)·MI, there is an intense (in MCD) low energy LF band (~5200 $cm^{-1}$) and a higher energy LF band (~11200 $cm^{-1}$) indicating that the Fe(II) site has become 5C square pyramidal upon MI binding. The VTVH MCD analysis also shows that $D_{Fe(II)}$ decreases from ~6 to ~4 $cm^{-1}$ upon MI addition, consistent with this 6C to 5C conversion. The increased splitting of the Fe(II) LF transitions upon decreased coordination allows the observation of a weak ferric spin-forbidden LF transition at ~8000 $cm^{-1}$. The low energy of this $^6A_1 \rightarrow {}^4T_1$ transition indicates a 6C ferric site. The VTVH MCD analysis shows that $-J$ also decreases upon MI addition (from ~12 to ~9 $cm^{-1}$) suggesting a weakened hydroxo-bridge. It should be noted that a previous analysis of the power saturation of the EPR intensity (Orbach relaxation), which measures the energy difference between the ground and excited state, showed a decrease in $-J$ from 20 to 10 $cm^{-1}$ upon MI addition to MIOX(II,III).[16] The study overestimated the magnitude and change in $J$ for two reasons: (1) ZFS was neglected, and (2) a conversion factor of ~0.7 $cm^{-1}$ $K^{-1}$ (Boltzmann's constant) was not included in the Orbach analysis. The decrease in the energy of the excited state upon MI binding is thus the result of both a decrease in the exchange coupling associated with a weakened hydroxo-bridge and a decrease in the ZFS of the Fe(II) reflecting the 6C to 5C Fe(II) structural change. Crystal structures have shown bidentate binding of MI to only one Fe.[16,18] It has been proposed that MI binds to the ferric site because it is a stronger Lewis acid and able to deprotonate the oxygen donor(s) of MI and activate the aliphatic group for H-atom abstraction and ring cleavage.[17,18] MI coordination to the Fe(III) is consistent with its 6C nature based on the $^4T_1$ LF transition energy. It should be noted that the two available crystal structures for MIOX have MI bound with both Fe sites 6C.[16,18] However, in one crystal structure, inosose-1 rather than inositol is bound, and in both structures, the oxidation state of the active site in the crystals was most likely biferric rather than the active Fe(II)Fe(III) species. Correlating the CD, MCD, and VTVH MCD data with the results of crystallography gives the structural model for MIOX(II,III)·MI shown in Figure 13C.

These structural models provide insight into the mechanism of MI binding and its activation of the $O_2$ reaction. The histidine-rich ligand field of MIOX results in a coordinatively saturated biferrous site that must be oxidized to the Fe(II)Fe(III) state to bind MI. The increased acidity of the Fe(III) leads to the formation of the $\mu$-$OH^-$ bridge and allows MI to bind (bidentate). The alkoxo groups on MI provide more electron donation and stronger binding to the Fe(III) than the replaced solvent due to increased basicity. This increased donation in turn weakens the Fe(III)−($\mu$-OH) bond. This change in bonding allows the bridging hydroxo to increase its electron donation to the Fe(II), which weakens the Fe(II)−$OH_2$ bond and leads to water loss, producing the observed 5C Fe(II) site that can react with $O_2$ by an inner-sphere mechanism. In addition to the structural change at the ferrous center, the increased charge donation from the bridged hydroxo to the Fe(II) would increase its oxidation potential and favor the one-electron reduction of $O_2$ to form the superoxide bound intermediate G that abstracts the C1−H from the substrate. Thus, rather than the more generally observed $2e^-$ reduction of $O_2$ by 2Fe(II) to form a peroxo intermediate for $2e^-$ electrophilic attack on a substrate, MIOX uses an Fe(II)Fe(III) site for $1e^-$ reduction of $O_2$ to form a superoxo intermediate for $1e^-$ H-atom abstraction.

## ■ ASSOCIATED CONTENT

### Supporting Information

The CD Fe(II) titration of MIOX, the overlay of the VTVH MCD of MIOX(II,II) with and without MI addition, the CD of MIOX(II,II), MIOX(II,III), and MIOX(II,III)·MI with and without sucrose addition, MCD spectra of MIOX(II,II), MIOX(II,III), and MIOX(II,III)·MI at different temperatures and magnetic fields showing C-term behavior, the CD of MIOX(II,III)·MI with different MI concentrations, close up of the CD of MIOX(III,III)·MI, the extended MCD spectra of MIOX(II,III) and MIOX(II,III)·MI, effective **g**-values of MIOX-(II,III) determined from the VTVH MCD shown on the EPR of MIOX(II,III), Mössbauer spectra of MIOX(II,II), MIOX-(III,III)·MI, and MIOX(II,III)·MI, and genetic algorithmic approach to fitting VTVH MCD data to eq 4. This material is available free of charge via the Internet at http://pubs.acs.org.

## ■ AUTHOR INFORMATION

### Corresponding Authors

jmb21@psu.edu
ckrebs@psu.edu
edward.solomon@stanford.edu

### Notes

The authors declare no competing financial interest.

## ■ ACKNOWLEDGMENTS

The NSF Biochemistry Program Grant (MCB-0919027 to E.I.S.) and the National Institutes of Health (Grant DK-074641 to J.M.B. and C.K.) provided financial support for this research.

## ■ REFERENCES

(1) Solomon, E. I.; Brunold, T. C.; Davis, M. I.; Kemsley, J. N.; Lee, S. K.; Lehnert, N.; Neese, F.; Skulan, A. J.; Yang, Y. S.; Zhou, J. *Chem. Rev.* **2000**, *100*, 235−349.
(2) Andrews, S. C. *Biochim. Biophys. Acta, Gen. Subj.* **2010**, *1800*, 691−705.
(3) Theil, E. C. *J. Nutr.* **2003**, *133*, 1549S−1553S.
(4) Shao, J.; Zhou, B.; Chu, B.; Yen, Y. *Curr. Cancer Drug Targets* **2006**, *6*, 409−431.
(5) Stubbe, J. *Curr. Opin. Chem. Biol.* **2003**, *7*, 183−188.
(6) Kokatnur, M. G.; Oalmann, M. C.; Johnson, W. D.; Malcom, G. T.; Strong, J. P. *Am. J. Clin. Nutr.* **1979**, *32*, 2198−2205.
(7) Yang, Y. S.; Broadwater, J. A.; Pulver, S. C.; Fox, B. G.; Solomon, E. I. *J. Am. Chem. Soc.* **1999**, *121*, 2770−2783.
(8) Lindqvist, Y.; Huang, W.; Schneider, G.; Shanklin, J. *EMBO J.* **1996**, *15*, 4081−4092.
(9) Howarth, R. W.; Santoro, R.; Ingraffea, A. *Clim. Change* **2011**, *106*, 679−690.
(10) Surampudi, S.; Narayanan, S. R.; Vamos, E.; Frank, H.; Halpert, G.; LaConti, A.; Kosek, J.; Prakash, G. K. S.; Olah, G. A. *J. Power Sources* **1994**, *47*, 377−385.
(11) Whittington, D. A.; Lippard, S. J. *J. Am. Chem. Soc.* **2001**, *123*, 827−838.
(12) Mitić, N.; Schwartz, J. K.; Brazeau, B. J.; Lipscomb, J. D.; Solomon, E. I. *Biochemistry* **2008**, *47*, 8386−8397.
(13) Lipscomb, J. D. *Annu. Rev. Microbiol.* **1994**, *48*, 371−99.
(14) Xing, G.; Hoffart, L. M.; Diao, Y.; Prabhu, K. S.; Arner, R. J.; Reddy, C. C.; Krebs, C.; Bollinger, J. M., Jr. *Biochemistry* **2006**, *45*, 5393−5401.
(15) Brown, P. M.; Caradoc-Davies, T. T.; Dickson, J. M.; Cooper, G. J.; Loomes, K. M.; Baker, E. N. *Acta Crystallogr., Sect. F: Struct. Biol. Cryst. Commun.* **2006**, *62*, 811−813.
(16) Thorsell, A. G.; Persson, C.; Voevodskaya, N.; Busam, R. D.; Hammarström, M.; Gräslund, S.; Gräslund, A.; Hallberg, B. M. *J. Biol. Chem.* **2008**, *283*, 15209−15216.
(17) Bollinger, J. M., Jr.; Diao, Y.; Matthews, M. L.; Xing, G.; Krebs, C. *Dalton Trans.* **2009**, *0*, 905−914.
(18) Brown, P. M.; Caradoc-Davies, T. T.; Dickson, J. M.; Cooper, G. J.; Loomes, K. M.; Baker, E. N. *Proc. Natl. Acad. Sci. U.S.A.* **2006**, *103*, 15032−15037.
(19) Arner, R. J.; Prabhu, K. S.; Thompson, J. T.; Hildenbrandt, G. R.; Liken, A. D.; Reddy, C. C. *Biochem. J.* **2001**, *360*, 313−320.
(20) Bustamante, E.; Pedersen, P. L. *Proc. Natl. Acad. Sci. U. S. A.* **1977**, *74*, 3735−3739.
(21) Eisenberg, F., Jr. *J. Biol. Chem.* **1967**, *242*, 1375−1382.
(22) Naccarato, W. F.; Ray, R. E.; Wells, W. W. *Arch. Biochem. Biophys.* **1974**, *164*, 194−201.
(23) Holub, B. J. *Annu. Rev. Nutr.* **1986**, *6*, 563−597.
(24) Berridge, M. J.; Irvine, R. F. *Nature* **1989**, *341*, 197−205.
(25) Zhang, X.; Majerus, P. W. *Semin. Cell Dev. Biol.* **1998**, *9*, 153−160.
(26) Dutton, G., Ed. *Glucuronic Acid, Free and Combined: Chemistry, Biochemistry, Pharmacology, and Medicine*; Academic Press: New York, 1966.
(27) Xing, G.; Diao, Y.; Hoffart, L. M.; Barr, E. W.; Prabhu, K. S.; Arner, R. J.; Reddy, C. C.; Krebs, C.; Bollinger, J. M., Jr. *Proc. Natl. Acad. Sci. U.S.A.* **2006**, *103*, 6130−6135.
(28) Xing, G.; Barr, E. W.; Diao, Y.; Hoffart, L. M.; Prabhu, K. S.; Arner, R. J.; Reddy, C. C.; Krebs, C.; Bollinger, J. M., Jr. *Biochemistry* **2006**, *45*, 5402−5412.
(29) Charalampous, F. C.; Lyras, C. *J. Biol. Chem.* **1957**, *228*, 1−13.
(30) Charalampous, F. C. *J. Biol. Chem.* **1959**, *234*, 220−227.
(31) Yang, B.; Hodgkinson, A.; Millward, B. A.; Demaine, A. G. *Int. J. Diabetes Mellitus* **2010**, *2*, 169−174.
(32) Moskala, R.; Reddy, C. C.; Minard, R. D.; Hamilton, G. A. *Biochem. Biophys. Res. Commun.* **1981**, *99*, 107−113.
(33) Deranieh, R. M.; He, Q.; Caruso, J. A.; Greenberg, M. L. *J. Biol. Chem.* **2013**, *288*, 26822−26833.
(34) Di Paolo, G.; De Camilli, P. *Nature* **2006**, *443*, 651−657.
(35) Croze, M. L.; Soulage, C. O. *Biochimie* **2013**, *95*, 1811−1827.
(36) Vucenik, I.; Shamsuddin, A. M. *J. Nutr.* **2003**, *133*, 3778S−3784S.
(37) Brand, A.; Richter-Landsberg, C.; Leibfritz, D. *Dev. Neurosci.* **1993**, *15*, 289−298.
(38) Haris, M.; Cai, K.; Singh, A.; Hariharan, H.; Reddy, R. *Neuroimage* **2011**, *54*, 2079−2085.
(39) Cimini, D.; De Rosa, M.; Schiraldi, C. *Biotechnol. J.* **2012**, *7*, 237−250.
(40) Wei, P. P.; Skulan, A. J.; Mitić, N.; Yang, Y. S.; Saleh, L.; Bollinger, J. M., Jr.; Solomon, E. I. *J. Am. Chem. Soc.* **2004**, *126*, 3777−3788.
(41) Liu, K. E.; Wang, D.; Huynh, B. H.; Edmondson, D. E.; Salifoglou, A.; Lippard, S. J. *J. Am. Chem. Soc.* **1994**, *116*, 7465−7466.
(42) Tong, W. H.; Chen, S.; Lloyd, S. G.; Edmondson, D. E.; Huynh, B. H.; Stubbe, J. *J. Am. Chem. Soc.* **1996**, *118*, 2107−2108.
(43) Bollinger, J. M., Jr.; Krebs, C.; Vicol, A.; Chen, S.; Ley, B. A.; Edmondson, D. E.; Huynh, B. H. *J. Am. Chem. Soc.* **1998**, *120*, 1094−1095.
(44) Yun, D.; García-Serres, R.; Chicalese, B. M.; An, Y. H.; Huynh, B. H.; Bollinger, J. M., Jr. *Biochemistry* **2007**, *46*, 1925−1932.
(45) Broadwater, J. A.; Ai, J.; Loehr, T. M.; Sanders-Loehr, J.; Fox, B. G. *Biochemistry* **1998**, *37*, 14664−14671.
(46) Pereira, A. S.; Small, W.; Krebs, C.; Tavares, P.; Edmondson, D. E.; Theil, E. C.; Huynh, B. H. *Biochemistry* **1998**, *37*, 9871−9876.
(47) Korboukh, V. K.; Li, N.; Barr, E. W.; Bollinger, J. M., Jr.; Krebs, C. *J. Am. Chem. Soc.* **2009**, *131*, 13608−13609.
(48) Murray, L. J.; García-Serres, R.; Naik, S.; Huynh, B. H.; Lippard, S. J. *J. Am. Chem. Soc.* **2006**, *128*, 7458−7459.
(49) McSorley, F. R.; Wyatt, P. B.; Martinez, A.; DeLong, E. F.; Hove-Jensen, B.; Zechel, D. L. *J. Am. Chem. Soc.* **2012**, *134*, 8364−8367.
(50) Sawyer, D. T. *Oxygen Chemistry*; Oxford University Press: New York, 1991; p 21.
(51) Hirao, H.; Morokuma, K. *J. Am. Chem. Soc.* **2009**, *131*, 17206−17214.
(52) Diao, Y. Mechanistic Study of *myo*-Inositol Oxygenase, Ph.D. Thesis, The Pennsylvania State University, University Park, PA, 2011.
(53) Solomon, E. I.; Pavel, E. G.; Loeb, K. E.; Campochiaro, C. *Coord. Chem. Rev.* **1995**, *144*, 369−460.
(54) Yang, Y. S.; McCormick, J. M.; Solomon, E. I. *J. Am. Chem. Soc.* **1997**, *119*, 11832−11842.
(55) Kato, H.; Taniguchi, M.; Kato, T. *Chem. Phys. Lett.* **1972**, *14*, 231−233.
(56) Kato, H. *J. Chem. Phys.* **1973**, *59*, 1732−1737.
(57) Holt, S.; Dingle, R. *Acta Chem. Scand.* **1968**, *22*, 1091−1096.
(58) Hatfield, W. E. *Inorg. Chem.* **1964**, *3*, 605−606.
(59) Drummond, J.; Wood, J. S. *J. Chem. Soc. D: Chem. Commun.* **1969**, *23*, 1373−1373.
(60) Zhang, Y.; Gebhard, M. S.; Solomon, E. I. *J. Am. Chem. Soc.* **1991**, *113*, 5162−5175.
(61) Deaton, J. C.; Gebhard, M.; Solomon, E. I. *Inorg. Chem.* **1988**, *28*, 877−889.
(62) McCormick, J. M.; Reem, R. C.; Solomon, E. I. *J. Am. Chem. Soc.* **1991**, *113*, 9066−9079.
(63) Westmoreland, T. D.; Wilcox, D. E.; Baldwin, M. J.; Mims, W. B.; Solomon, E. I. *J. Am. Chem. Soc.* **1989**, *111*, 6106−6123.
(64) Creutz, C. In *Mixed Valence Complexes of d5-d6 Metal Centers*; Lippard, S. J., Ed.; Progress in Inorganic Chemistry: An Appreciation of Henry Taube; John Wiley & Sons, Inc.: Hoboken, NJ, USA, 1983; Vol. *30*, pp 1−73.
(65) Truesdale, G. A.; Downing, A. L.; Lowden, G. F. *J. Appl. Chem.* **1955**, *5*, 53−62.
(66) Neese, F.; Solomon, E. I. *Inorg. Chem.* **1999**, *38*, 1847−1865.
(67) Piepho, S.; Schatz, P. N. *Group Theory in Spectroscopy: With Applications to Magnetic Circular Dichroism*; John Wiley & Sons, Inc.: New York, 1983.

(68) Stephens, P. *Annu. Rev. Phys. Chem.* **1974**, *25*, 201−232.
(69) Bennett, D. E.; Johnson, M. K. *Biochim. Biophys. Acta, Protein Struct. Mol. Enzymol.* **1987**, *911*, 71−80.
(70) Solomon, E. I.; Kirk, M. L.; Gamelin, D. R.; Pulver, S. *Methods Enzymol.* **1995**, *246*, 71−110.
(71) Guigliarelli, B.; Bertrand, P.; Gayda, J. P. *J. Chem. Phys.* **1986**, *85*, 1689−1692.